GEOPHYSICS, VOL. 74, NO. 6 (NOVEMBER-DECEMBER 2009); P. WCC69–WCC77, 14 FIGS.
10.1190/1.3223315

Effects of surface scattering in full-waveform inversion

Florian Bleibinhaus[1] and Stéphane Rondenay[2]

ABSTRACT

In full-waveform inversion of seismic body waves, often the free surface is ignored on grounds of computational efficiency. A synthetic study was performed to investigate the effects of this simplification. In terms of size and frequency, the test model and data conform to a real long-offset survey of the upper crust across the San Andreas fault. Random fractal variations are superimposed on a background model with strong lateral and vertical velocity variations ranging from 1200 to 6800 m/s. Synthetic data were computed and inverted for this model and different topographies. A fully viscoelastic time-domain code was used to synthesize the seismograms, and a viscoacoustic frequency-domain code was utilized to invert them. The inversion was focused on early arrivals, which are dominated by P-waves but also contain strong P-Rayleigh wave conversions from the near-field of the receiver. Resulting waveform models show artifacts and a loss of resolution from neglecting the free surface in the inversion, but the inversions are stable, and they still improve the resolution of kinematic models. The extent of deterioration depends more on the subsurface than on the surface structure. Inversion results were improved at no additional expense by introducing a weak contrast along a staircase function above shots and receivers.

INTRODUCTION

Computational expense of the forward solution is one of the most critical issues in waveform inversion. For practical applications, severe simplifications must be employed to make the inversion feasible. In controlled-source seismology, the most popular forward solutions are 2D, isotropic, acoustic or viscoacoustic, and FD frequency-domain methods (e.g., Hicks and Pratt, 2001; Operto et al., 2004; Ravaut et al., 2004; Operto et al., 2006; Bleibinhaus et al., 2007; Gao et al., 2007; Malinowski and Operto, 2008). Validity of this approximation has been established by a study on a physical scale model by Pratt (1999). However, the actual limitations arising from such extensive approximations are not well understood.

This lack of understanding prompted a series of synthetic studies, e.g., to investigate the degradation from inverting elastic phases in the acoustic approximation (Barnes and Charara, 2008; Choi et al., 2008), or to study the impact of attenuation and the possibility of retrieving attenuation structure (Kamei and Pratt, 2008). Our objective is to evaluate the effects of neglecting the free surface in acoustic full-waveform inversion. All of the above-mentioned practical applications of controlled-source full-waveform inversion ignore the free surface, embed shots and receivers in the model, and remove surface-related phases from the data as much as possible. This is done mostly because implementing a complex topography is quite expensive computationally. Considering that the next step in controlled-source full-waveform inversion is the extension to 3D acoustic (Virieux et al., 2009), the computational demands of including topography will not shrink in the near future.

However, Hicks and Pratt (2001) and Operto et al. (2006) also argue that full-waveform inversion becomes unstable when faced with free-surface multiples. They, too, exclude the surface-related phases from the inversion and use an absorbing boundary on top of the model, even though they invert marine data and they could implement a flat surface at no cost. This aspect underscores the necessity to study the impact of neglecting the free surface in more detail, before attempting to implement it into the inversion scheme.

The primary motivation for this study came from the full-waveform inversion of long-offset data collected in an area with strong topography across the San Andreas fault (Bleibinhaus et al., 2007). They do not account for free-surface effects, although the seismic shot records appear strongly scattered because of rough topography, and comprise reverberations and conversions from the surface (Figure 1).

We tried to obtain a preliminary estimate of the degrading effect of neglecting the free surface by comparing frequency-domain wavepaths computed with and without a free, irregular surface (Figure 2).

Manuscript received by the Editor 30 January 2009; revised manuscript received 22 May 2009; published online 3 December 2009; corrected version published online 17 December 2009.
[1]Formerly Massachusetts Institute of Technology, Department of Earth, Atmospheric, and Planetary Sciences, Cambridge, Massachusetts, U.S.A.; presently University of Salzburg, Geology Department, Salzburg, Austria. E-mail: florian.bleibinhaus@sbg.ac.at.
[2]Massachusetts Institute of Technology, Department of Earth, Atmospheric, and Planetary Sciences, Cambridge, Massachusetts, U.S.A. E-mail: rondenay@mit.edu.

We computed these wavepaths from the frequency-domain source and receiver wavefields. For the wavepath of Figure 2b, first we computed the pressure field from the divergence of the particle velocity after Dougherty and Stephen (1988). Then the frequency-domain wavefields were computed with the phase-sensitive detection method after Nihei and Li (2007): we used a harmonic signal to drive the time-domain shot and receiver wavefields into a steady state, and then we performed a DFT over one cycle at 4 Hz for each subsurface point. The result can be compared directly to the acoustic wavepath in Figure 2a. The difference between them is huge. However, this is primarily a result of surface waves, which dominate the fully elastic wavepath of Figure 2b. Because surface waves were excluded from the inversion by Bleibinhaus et al. (2007), this is not a meaningful comparison. To reduce the impact of surface waves on the fully elastic wavepath, we computed a third wavepath using a finite (Ricker) wavelet and running the DFT for 25 cycles from $t = 0–6.25$ s. This amount of time is required to record the early arrivals that were actually used in the inversion. The resulting wavepath (Figure 2c) is dominated by P-waves and P-Rayleigh conversions from the vicinity of source and receiver. Compared to the acoustic wavepath of Figure 2a, it shows a similar first-order structure, with a central lobe that is ~2-km wide. However, it also shows strong scattering, and the outer fringes are distorted heavily. Although much of these small-scale variations would be suppressed during the inversion by regularization filters, the differences appear significant enough to assume that ignoring them could cause strong artifacts. Unfortunately, the central section of the wavepath of Figure 2c is still influenced by direct surface waves, because this is how far they get from the shot and from the receiver in 6.25 s. This limits the significance of the comparison.

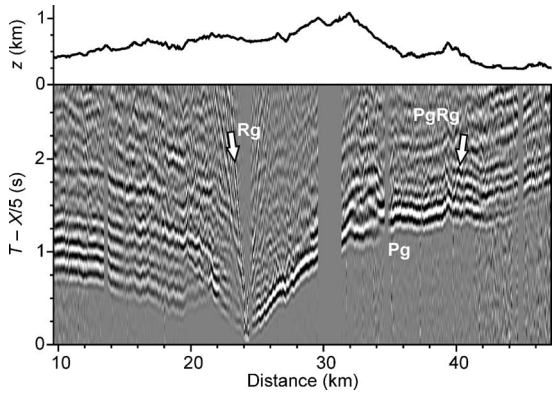

Figure 1. Trace-normalized time-reduced vertical-component shot gather from the San Andreas fault survey, elevation on top, vertical exaggeration is 5. The data are 14-Hz low-pass filtered, such that they can be compared to the synthetic data in this study. Rg denotes the Rayleigh wave, Pg is the crustal direct P-wave, PgRg is the P-wave to Rayleigh wave conversion.

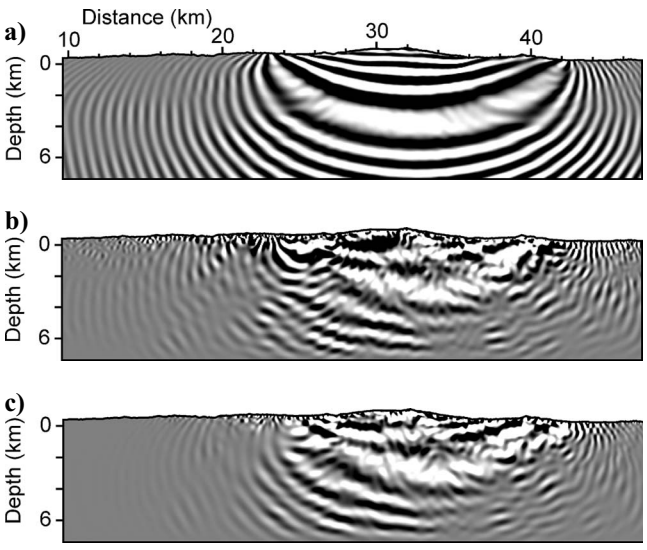

Figure 2. Monochromatic 4-Hz-pressure wavepaths for one source-receiver pair computed in the smooth waveform inversion starting model of Bleibinhaus et al. (2007) for constant attenuation ($Q = 50$) with (a) the viscoacoustic frequency-domain code of Pratt (1990; 1998) using absorbing boundaries above the receivers, and (b, c) with the viscoelastic time-domain code of Robertsson (1996) and a free surface with irregular topography. (c) A time window is applied.

To investigate the impact of free-surface effects on acoustic full-waveform inversion, this study proceeds as follows. First we created synthetic data for a model with a flat surface and for a model with irregular topography. To account for all surface-related phases, we used a fully viscoelastic code to generate the data. Then we inverted these data with a different, acoustic wave propagator optimized for full-waveform tomography. We computed two inversions for each data set, one with an absorbing boundary on top of the model, and one with a free surface. Naturally, it is impossible to reproduce fully elastic data with an acoustic code, and all inversion results suffer from this deficiency. However, the amount of degradation from inverting irregular-topography data as opposed to flat-surface data can be deduced from comparing the different inverse models. In addition, the amount of degradation from using an absorbing boundary on top of the model as opposed to a free surface can also be deduced.

TEST MODEL

To investigate the effects of scattering from topography in acoustic full-waveform inversion, we generated and inverted synthetic test data with and without topography. Our test model is a superposition of fractal velocity variations of ± 800 m/s onto a background model that reflects the complex structure across the San Andreas fault in central California (Figure 3). The resulting P-wave velocity range is 1.2–6.8 km/s. The strong discontinuity in the left part of the model (<25 km) represents a contact of sediments over granite, and the background structure essentially resembles a layer over a half-space. In contrast, the right part of the model (>25 km) represents a sedimentary mélange, and the background is dominated by a constant vertical gradient. The S-wave distribution is a scaled version of the P-wave model, with additional random long-wavelength perturbations, such that V_P/V_S ranges from 1.5 to 1.9.

The Q-distribution is similar to the background velocity model, and Q_S was set to $Q_P/2$. The average Q_S (Q_P) in our model is 790 (1580) in the upper 2 km, and 1260 (2520) in the upper 4 km, resulting in ~10% (3%) attenuation of S-wave (P-wave) amplitudes after a distance of 10 km. This corresponds to relatively weak attenuation. To account for the strong attenuation observed at the San Andreas fault (Bleibinhaus et al., 2007), we made another model in which Q is decreased by 90%. However, we put the weakly attenuating model in the foreground of this study, because the strong attenuation could mitigate the effects of surface-scattered waves.

Densities were derived from the velocity model using Gardner's formula (Gardner et al., 1974), and adding 3% random variations.

The model size is 2501×501 grid nodes with a regular spacing of 15 m. The resulting model exhibits a fair amount of heterogeneity on all scale lengths. It represents a complex geological situation that is difficult to image. In particular, the layer-over-half-space (left) part of the model will prevent deep penetration, and create strong multiples and reverberations that should have a significant impact on the waveforms.

Two models were derived from the parameter distributions displayed in Figure 3 by adding a free surface, either at a constant level of 750 m, or at an elevation varying from 200 m to 1100 m above sea level (Figure 1). Figure 4 shows the wavenumber spectrum of this topography and other mountain ranges to give an impression of the roughness. Note that all elevation profiles show a red spectrum ($A \sim \lambda$), as is typical for most physical surfaces (Sayles and Thomas, 1978). The constant ratio of the amplitude A of height variations to their wavelength λ ensures the results of this study are scalable. Surface effects would not be stronger or weaker at higher or lower frequencies.

SYNTHETIC DATA

Synthetics were generated with the viscoelastic finite-difference time-domain code of Robertsson et al. (1994), Robertsson (1996), and Robertson and Holliger (1997). It accounts for an irregular free surface using the image method (Levander, 1988), where certain components of stress and particle velocity are imaged as odd functions in the vicinity of the free surface. We used a 5-Hz Ricker wavelet as the source. The relative amplitude of the wavelet drops below 10^{-5} at 20 Hz, corresponding to a 100-m wavelength at 2000 m/s (Figure 4). This is the smallest wavelength we took into account, and it determines the maximum grid spacing required to compute accurate solutions.

Benchmark tests by Robertsson (1996) suggest that an irregular surface must be sampled by at least 15 grid points per minimum wavelength. Bohlen and Saenger (2006), who developed a similar viscoelastic 3D code, conclude from their benchmark tests that at least 60 grid points per minimum wavelength would be required to avoid edge effects from the gridded irregular topography. These estimates are based on the accuracy of surface waves. However, for the inversion of the early arrivals, it suffices to tailor the grid spacing to the accuracy of P-waves. To estimate the inaccuracy, we compared solutions for a grid spacing of 10, 5, and 2.5 m, corresponding to 10, 20, and 40 samples per shortest P-wavelength, respectively. At 2.5 m, the grid consists of 1.4×10^7 grid nodes, and synthesizing one data set amounts to six months of CPU time. In terms of memory, CPU time, and numerical dispersion, 2.5-m grid spacing poses a practical limitation. To compare the solutions, we compute the rms difference of trace-normalized amplitudes in a 1.5-s-long window after the P-wave first arrival at offsets greater than 2.5 km, such that direct surface waves are excluded. This difference decreases from 50% to 10% when comparing the solutions for 10 and 5 m, and for 5 and 2.5 m, respectively. The difference between the 5-m data and the 2.5-m data is dominated by P-Rayleigh conversions in the vicinity of the receivers, suggesting that 2.5-m spacing (or 40 grid points per wavelength) still might not be accurate enough if we were to use these phases in the inversion. However, this difference is less than 5% for P-waves. This indicates that the major contribution to the error arises from the coarse sampling of the irregular surface, not from coarse sampling of subsurface heterogeneities. For example, the strong vertical contrast of sediments over basement between 20 and 25 km is sampled by ~20 nodes at 5-m spacing. Below this contrast, the grid spacing was tripled to save computation time. For computational reasons, we synthesized the data at a spacing of 5 m. To assess the influence of the numerical error, we also generated and inverted one data set with topography at 2.5-m spacing.

We computed 76 shot sections at 500-m spacing for a 37.5-km-long stationary receiver array at 50-m spacing for a model with a flat surface and for a model with irregular topography (Figure 5). The major difference from the real data (Figure 1) is the surface waves, which almost are not attenuated in the synthetics. However, the amount of scattering in the real data and the irregular-topography synthetics is similar.

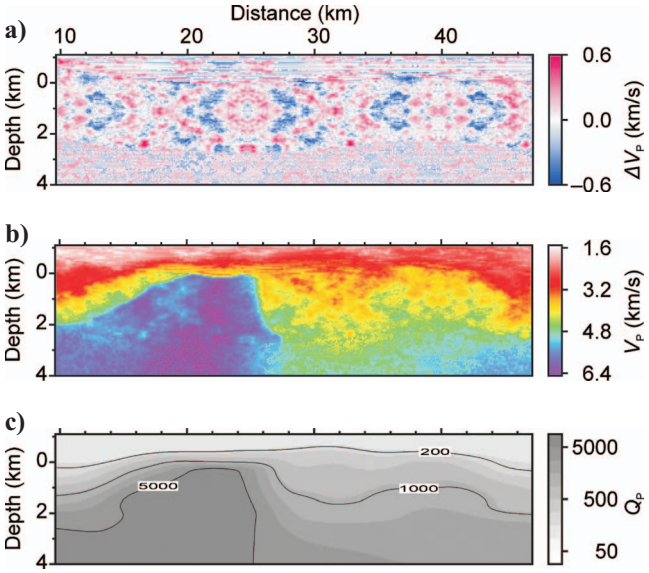

Figure 3. Synthetic test model: (a) fractal perturbations, (b) P-wave velocity, and (c) Q_P.

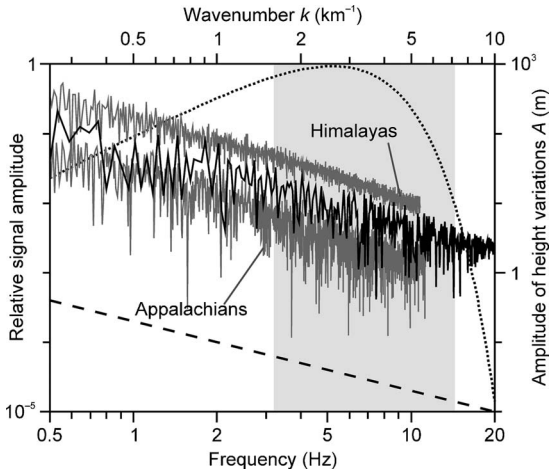

Figure 4. Wavenumber spectrum of the topography (solid black) and frequency spectrum of the 5-Hz Ricker source wavelet (dotted), related through a constant velocity of 2000 m/s. The shaded area denotes frequencies used in the waveform inversion. For comparison, gray lines show the spectra for elevation profiles across the Himalayas near Mt. Everest and across the Appalachians in Virginia computed from 3″ shuttle radar data provided by the U.S. Geological Survey. Dashed line denotes a decay $\sim 1/k$.

To prepare these data for acoustic full-waveform inversion, we applied windows in space (only offsets greater than 2.5 km) and time (only until 1.5 s after the first break) to exclude surface waves, shear waves, and late arrivals (Figure 6). In addition, we applied an exponential amplitude decay with a half-value of 1 s to avoid artifacts from the time windowing. The remaining energy corresponds mostly to forward-scattered P-waves.

STARTING MODEL

Wavelengths that can be resolved by full-waveform inversion are closely related to the bandwidth of the data. In particular, low frequencies are required to resolve the long-wavelength structure of the model. Pratt et al. (1996) show that for full-waveform inversion to converge towards the global minimum, the long-wavelength structure of the background starting model must not be erroneous beyond what can be resolved by the lowest data frequencies. Typically, real applications derive starting models from traveltime tomography. We could have used a filtered version of our synthetic model instead, but we preferred to employ traveltime tomography to be more realistic. We performed a damped least-squares inversion, using the eikonal solver of Hole (1992) to compute first-arrival times. Observed times could be picked automatically because our synthetics are noise-free. The inversion grid was adjusted to the resolving power of the data by iteratively removing nodes, if their resolution diagonal element falls below a threshold of 0.2. The rms residual drops from 0.5 to 0.01 s within five iterations. We achieved a resolution of 0.25/1 km (vertical/lateral) near the surface, which decreases to ~0.5/2 km at greater depth (Figure 7). Varying penetration depth and resolving power in the different parts of the model are reflected by the density of the inversion nodes. As a final step to obtaining a starting model for full-waveform inversion, the velocity values in areas without ray coverage were replaced by extrapolation. For convenience, we performed traveltime tomography only for the flat-surface data set. A starting model for the irregular topography data was derived by adding the uppermost portion of a filtered version of the true model on top of the flat-surface tomography results. The filter was designed to remove wavelengths shorter than 0.25/1 km, such that the resolution corresponds to the upper section of the traveltime tomography model.

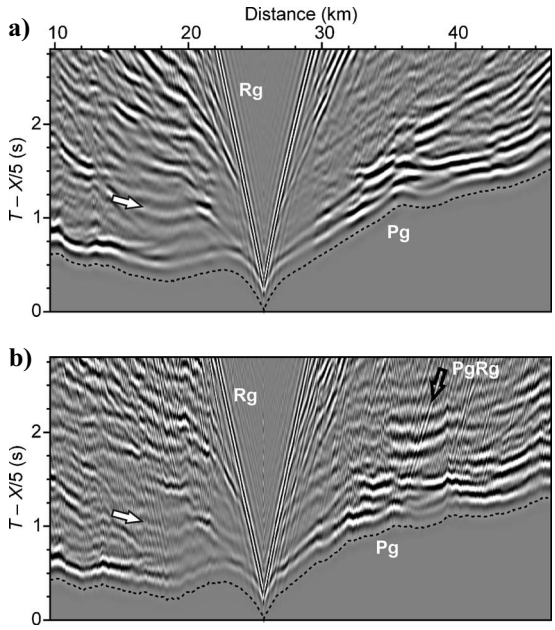

Figure 5. Trace-normalized, 5-Hz high-pass-filtered, reduced shot sections at 26 km, vertical component (a) computed for a flat surface, and (b) for irregular topography. In addition to the significant scattering in (b), several phases differ strongly between the sections (white arrows). Rg denotes the Rayleigh wave, Pg is the crustal direct P-wave, and PgRg is the P-Rayleigh wave conversion at the free surface. Dotted line represents first-arrival picks.

WAVEFORM INVERSION

Inversion strategy

Our full-waveform inversion strategy is almost identical to the one described by Bleibinhaus et al. (2007). We used a multiscale approach to mitigate the nonlinearities inherent to full-waveform inversion (Bunks et al., 1995; Pratt et al., 1996). To reconstruct the model from coarse to fine wavelengths, we inverted increasingly higher frequencies sequentially from 3.2 to 14.4 Hz. Seven nonoverlapping narrow bands were chosen, each comprising three frequency components. Our inverse model grid consists of 1541 × 341 nodes at a spacing of 25 m. For the cost function, we used the difference between the phase of the vertical component of the particle velocity and the phase of the pressure computed with the viscoacoustic frequency-domain code of Pratt and Worthington (1990) and Pratt et al.

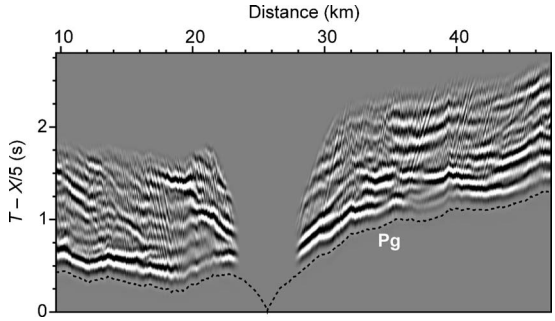

Figure 6. Preprocessed, trace-normalized shot gather of Figure 5b, vertical component. Traces were muted 1.5 s after the first arrivals with a 200-ms taper, and the near offsets (2.5 km) were excluded from the inversion. Remaining shear waves in the offset range of 2.5–5 km were removed by an offset-dependent mute window. Pg is the crustal direct P-wave. Dotted line represents first-arrival picks.

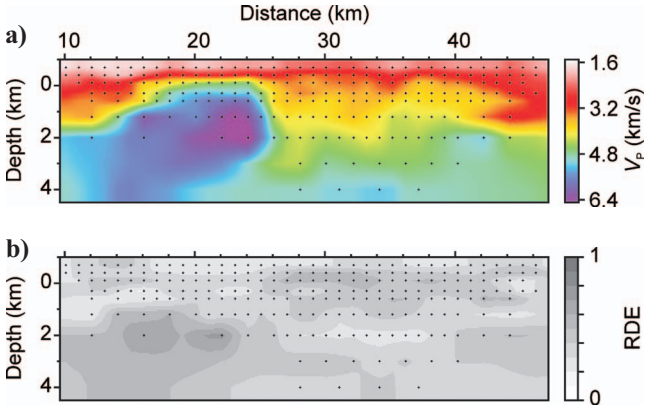

Figure 7. (a) P-wave velocity model from traveltime tomography, and (b) corresponding diagonal elements of the resolution matrix. Black dots are inversion nodes.

(1998). The systematic differences between these signals comprise a constant phase shift arising from their derivative relation that is accounted for implicitly by the source term (Operto et al., 2004), and a more complex amplitude difference of no consequence for this study because we inverted the phase only. We did not invert the amplitudes because we wanted to use the same objective function that Bleibinhaus et al. (2007) uses for inversion of the real data. They argue that real data amplitudes are too strongly affected by variations of near-surface attenuation and coupling conditions. In addition, the amplitudes are sensitive only to the spatial gradient of the velocities, not to the velocities themselves, and their resolving power is relatively poor compared to the phase, as is demonstrated by Shin and Min (2006).

Model updates were computed with the steepest descent method, and the gradient was calculated by interference of the source wavefield with back-propagated residuals. For the sake of computational efficiency, we did not perform a full line search to find the optimum step length. Rather, we accepted the first step length that led to a residual reduction, and then proceeded to the next iteration. From empirical tests, we found that five iterations are required to descend to the minimum in most cases. We used a common, isotropic source for all shots. We derived the source signature separately for each frequency band by a subspace inversion before the first iteration. Adding subsequent inversions for the source did not improve the results.

Surface boundary condition

We computed two inversions for each data set, one with an absorbing boundary on top of the model, and one with a surface above the receivers. We denote these inversions in shorthand as absorbing boundary, and free surface, respectively. For absorbing-boundary inversions, receivers and shots were embedded in the model at a minimum distance of 10 nodes from the top boundary, and the material properties were extrapolated above ground. For the free-surface inversion of the flat-surface data, we employed an explicit boundary condition. For the irregular-topography data, we parameterized the surface with a staircase function, above which we set the material properties to a different value. This implicit formulation is not correct because our algorithm does not account for spatial heterogeneity explicitly. Hence, we could not introduce a strong discontinuity at the staircase function. Instead, we reduced the velocity by 50% and the density by 20%, the latter being computed automatically from the P-wave velocities using Gardner's formula. The staircase is as close as possible to the real surface, but still far enough above ground so that each receiver is surrounded entirely by subsurface nodes. On average, the resulting model surface is at least one grid node above the real surface, and this gives rise to a spurious reflection. However, because this effect is relatively constant for all shots and receivers, it is accounted for in the source signature. The resulting seismograms reflect some amount of surface scattering, and in contrast to seismograms computed with an absorbing boundary on top of the model, they show no indication of wave propagation above ground (Figure 8).

Inversion results

Figures 9 and 10 display a comparison of the inverse models with the starting model and the true model. All waveform models increase the resolution of the traveltime model significantly, whether they were derived from flat-surface data or from irregular topography data, and whether or not they respect the free-surface condition. Many details of the original model have been reconstructed. Resolution is generally better in the gradient (right) part of the model. In some instances, the amplitude of perturbations is underestimated, and their location is not fully congruent with the true model. The layer-over-half-space (left) part of the model is less well resolved. Velocities just below the discontinuity are overestimated, and the internal structure of the half-space is distorted. The strong anomaly at 20 km laterally and a depth of 1 to 1.5 km (Figure 10) is still imaged, but no structures could be recovered below a depth of 2 km, where the large mismatch of the starting model is not corrected by the inversion.

On closer inspection, the inverse models show some significant differences. The absorbing-boundary inverse models exhibit artifacts at shallow depth, and the model fit is clearly inferior. In the layer-over-half-space (left) part of the model, the absorbing-boundary reconstruction from flat-surface data fails (Figure 10, at 20 km). Overall reduction of the rms-model misfit (Figure 11) confirms that the absorbing-boundary inversions generally produce inferior results.

These statistics do not show that the inverse models from the irregular-topography data of Figure 9d and e are generally worse than the inverse models from the flat-surface data of Figure 9b and c. Indeed, in the constant-gradient (right) part of the model, the differences are insignificant. In the layer-over-half-space (left) part of the model, the degradation from ignoring the free surface is worse for

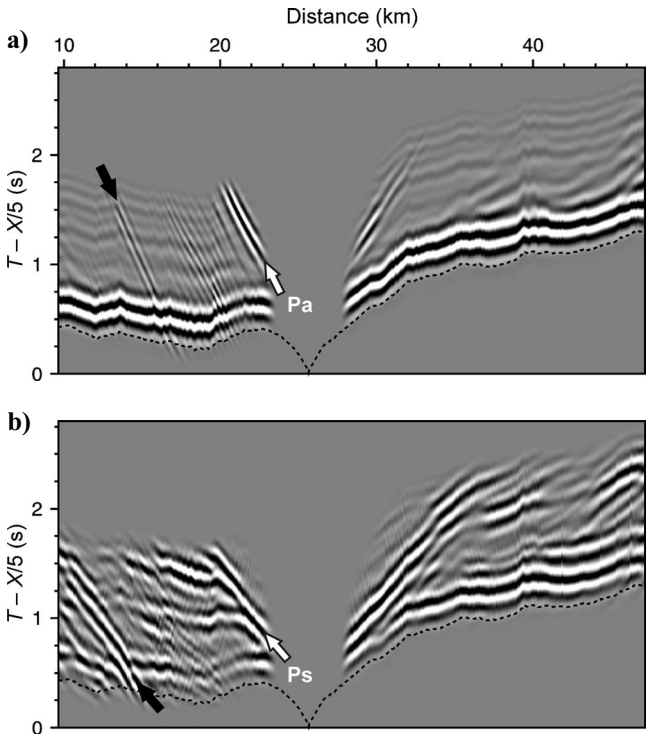

Figure 8. Trace-normalized, reduced and windowed seismogram section computed for the starting model with topography using the acoustic frequency-domain code of Pratt (1999) with (a) an absorbing boundary on top of the model and (b) an additional weak contrast along a staircase function. Note the very slow, artificial P-wave Pa in (a), which partially propagates above ground. The direct P-wave Ps in (b) propagates in the slow layer over the half-space. Time aliasing (black arrows) is a result of the inverse Fourier-transformation and is of no consequence for the inversion. Dotted line represents first-arrival picks.

flat-surface data than for irregular-topography data. However, this difference is also affected by the different surface boundary conditions. In any case, there is no indication that ignoring the free surface in full-waveform inversion of P-waves is generally worse when the topography is rough. Another result is that modeling the free surface improves the inversions, even if it is only a weak, implicit boundary condition. A comparison of seismograms also confirms this (Figure 12). All shot sections are closer to the original data of Figure 5, especially in the right part of the model (e.g., note the reconstruction of the relatively low amplitudes of the first arrival at 36–40 km). However, the data computed in the absorbing-boundary inverse model still shows the spurious phase Pa that was already present in the starting model (Figure 8a), and that hampers the reconstruction especially in the left part of the model. This is not the case for the implicit-surface inverse model, which matches the original data (Figure 5b) much better, particularly when computed with the fully elastic wave-propagator and an explicit free surface (Figure 12c). Comparison of the acoustic reconstruction of Figure 12b with the original data also shows that the P-Rayleigh conversions are not mapped into the model space.

Figure 13 displays a summary of the rms-phase-misfit reduction for all inversions. The overall misfit reduction ranges from 20% to 40%, and the trends are similar for all inversions in that the reduction is stable and monotonous. The absolute differences arise from different data sets and boundary conditions.

A more detailed view of the misfit reduction is given in Figure 14. It shows that the inversion of a certain frequency band also reduces the misfit at much higher frequencies, which is an indication of the

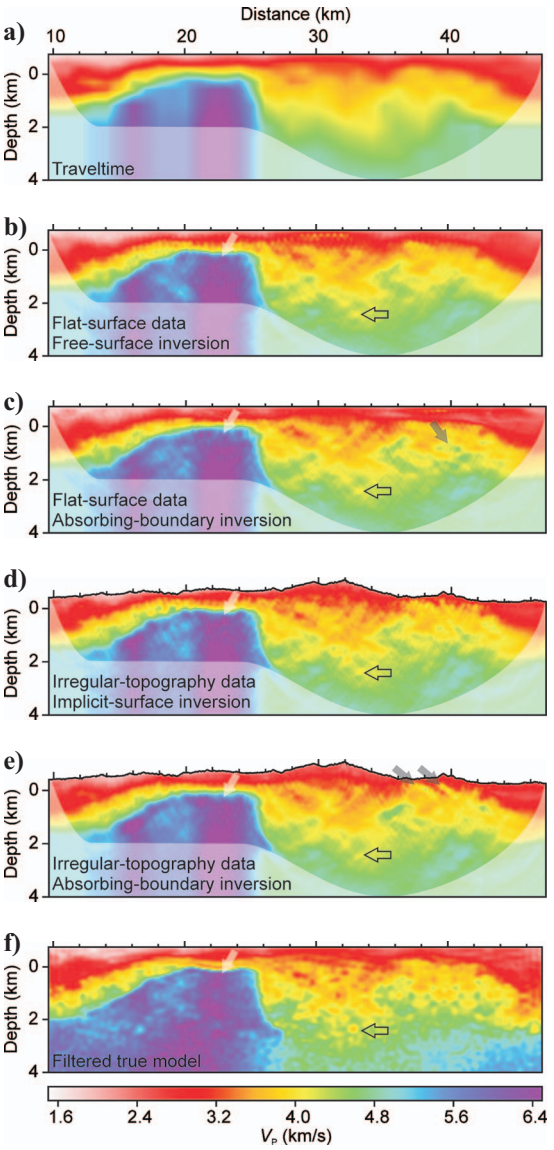

Figure 9. (a) Starting model for full-waveform inversion derived by traveltime tomography, (b-e) full-waveform inversion models, (f) filtered true model. (b and c) Models derived from flat-surface data, and (d and e) models derived from irregular-topography data; (b, d) account for the surface, and (c, e) use an absorbing boundary on top of the model. Whitish area is low subsurface coverage. Many structures, even at small scales, are recovered by all inversions (see hollow arrows, for example). However, the sharp contrast of sediments over granite is not very well recovered in either case (white arrow). Note that the absorbing-boundary inversions of both data sets (c, e) show some additional shallow artifacts (gray arrows).

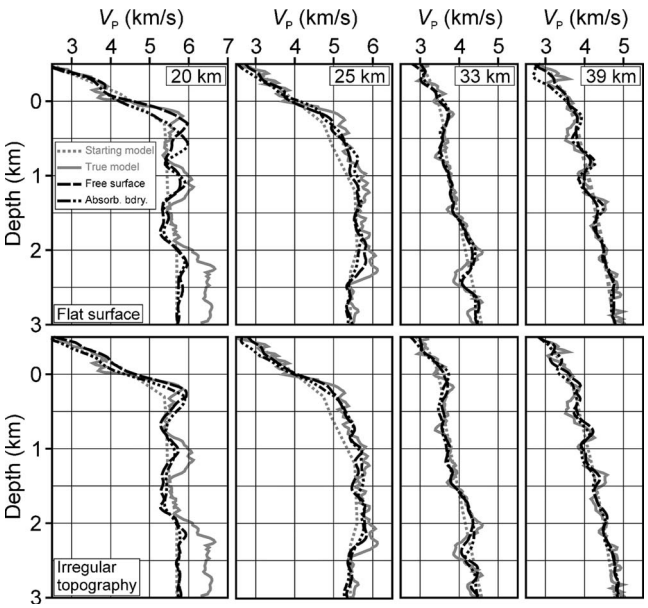

Figure 10. $V(z)$ functions for the models of Figure 9 computed from the flat-surface data (top panels) and irregular-topography data (bottom panels). Gray lines are starting model (dotted) and true model (solid), black lines are free-surface inverse models (dashed) and absorbing-boundary inverse models (dash-dotted). The left panels at distances of 20 and 25 km correspond to the layer-over-half-space part of the model, and the right panels at distances of 33 and 39 km correspond to the constant-gradient portion.

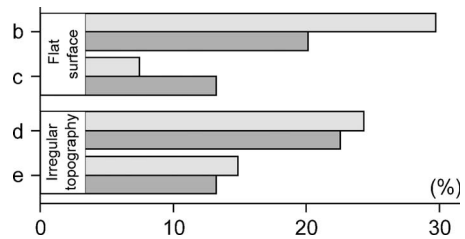

Figure 11. Relative rms-velocity misfit reduction for the waveform models of Figure 9b-e. Light bars denote the layer-over-half-space (left) part of the model; dark bars denote the gradient-layer (right) part of the model.

stability of the inversion. After the final inversion step (Figure 14d), the match at 12–14 Hz is slightly better compared to 10–12 Hz. Bleibinhaus et al. (2009) also observe this in the inversion of the real data, and it indicates that the inversion converged toward a local minimum. To avoid it, we tried to re-invert one component of each low-frequency band along with the high-frequency bands. However, we found that the convergence was compromised and, overall, the results were inferior. Another feature of the phase diagrams in Figure 14 is that the higher the frequency, the larger the residual at long offsets. This could indicate the predominance of multiple scattering: a propagation distance of 25 km corresponds to ~50 wavelengths at 10 Hz. It is likely that such a wave is scattered more than once, thus increasing the nonlinearity of the inversion.

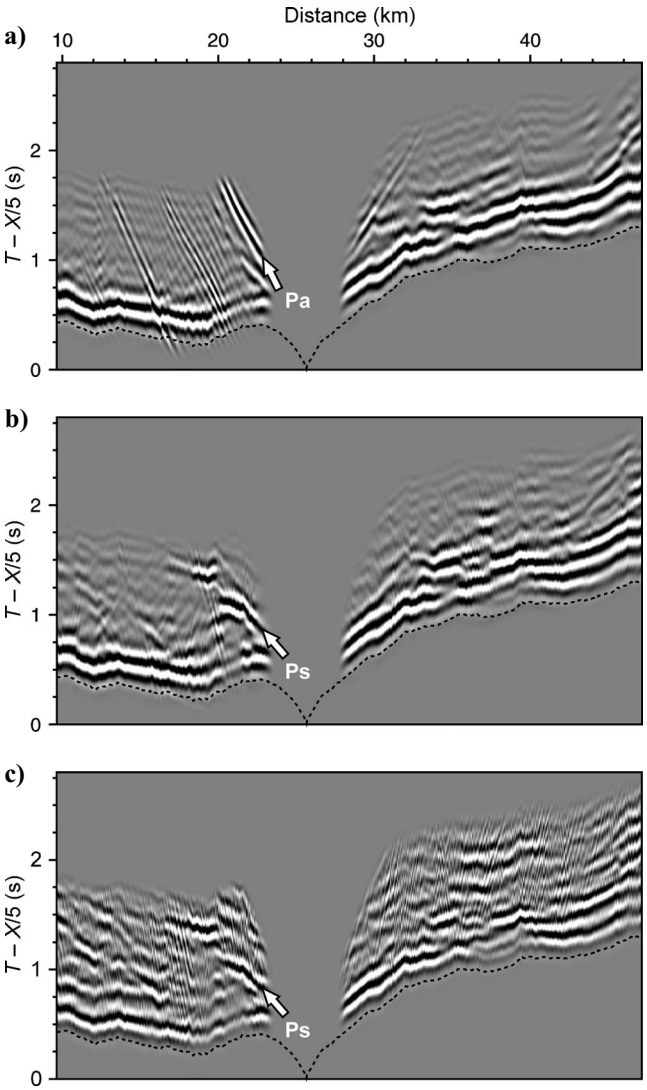

Figure 12. Trace-normalized shot gathers for irregular topography computed (a) in the absorbing-boundary inverse model of Figure 9e, and (b, c) in the implicit-surface inverse model of Figure 9d. The pressure data were computed with the viscoacoustic frequency-domain code and (a) an absorbing boundary on top of the model, and (b) an implicit free surface. (c) Vertical-component data computed with the viscoelastic time-domain code and an explicit free surface. Pa is the artificial P-wave propagating above ground, and Ps is the direct P-wave propagating in the slow layer over the half-space. Dotted line represents first-arrival picks.

DISCUSSION

It is noteworthy that the data and model misfits after acoustic waveform inversion are still relatively large for all inverse models. For the data, the misfit reduction is 20–40%, and for the models, 10–30%. To ensure that the inaccuracy of our test data was not responsible, we compared inversions from data generated with 2.5-m spacing and with 5-m spacing. Inverse models from the 2.5-m data are indeed ~10 m/s closer to the true model, but this is a relatively small amount. Qualitatively, the models look identical, even the artifacts. This assures us that the impact of numerical inaccuracy of the synthetic data on our results is minor. Other reasons explain the large residuals. First, it is impossible to match fully elastic data with an acoustic code. Our data preparation attempted to focus on acoustic phases, but near-field conversions from the surface and the subsurface are inevitably superposed on this data, and they are not reproduced in the acoustic approximation, as illustrated in Figure 12. Most scattering in the elastic data of Figure 12c is the result of P-Rayleigh conversions, and it could not be reproduced in the acoustic approximation even with a perfect boundary condition. Second, the model required to explain the data has density and V_S perturbations that cannot be reproduced in the acoustic approximation. Third, we did not use a wavenumber-filtered version of the true model as the starting model. Instead, we derived it from traveltime tomography, resulting in long-wavelength misfits, particularly in the left part of the model. These misfits persist partially throughout the inversion, because the penetration in this part of the model is too shallow. We also tested to find out if a lower starting frequency could remove them. However, inversions starting at 1 Hz and at 2 Hz improved the overall match by another ~5% only, and they did not remove those large initial misfits. As a result, the imaged perturbations are not always congruent with the true model, which increases the mismatch significantly.

All these deficiencies are essentially the result of using relatively realistic data for the inversion. However, there are still two major

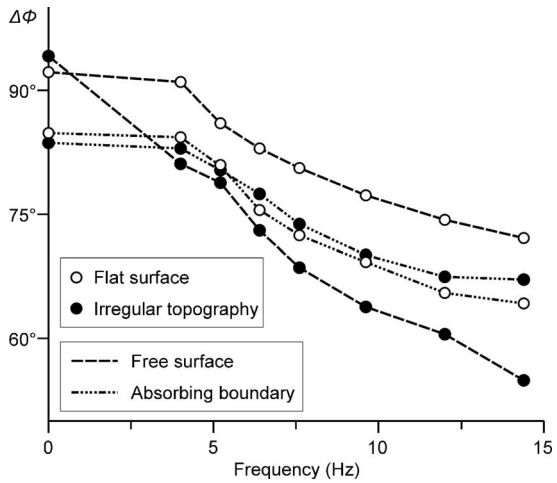

Figure 13. Root-mean-square-phase misfit reduction plotted against the highest frequency of the inverted band. The misfit is computed for the whole inverted spectrum (3.2–14.4 Hz), but the objective function of each inversion step encompasses a narrow band only. Hollow circles are flat-surface data, and black circles are irregular-topography data. Dashed lines represent free-surface inversions, and dash-dotted lines are absorbing-boundary inversions. The misfit reduction at 14.4 Hz corresponds to the models of Figure 9b-e.

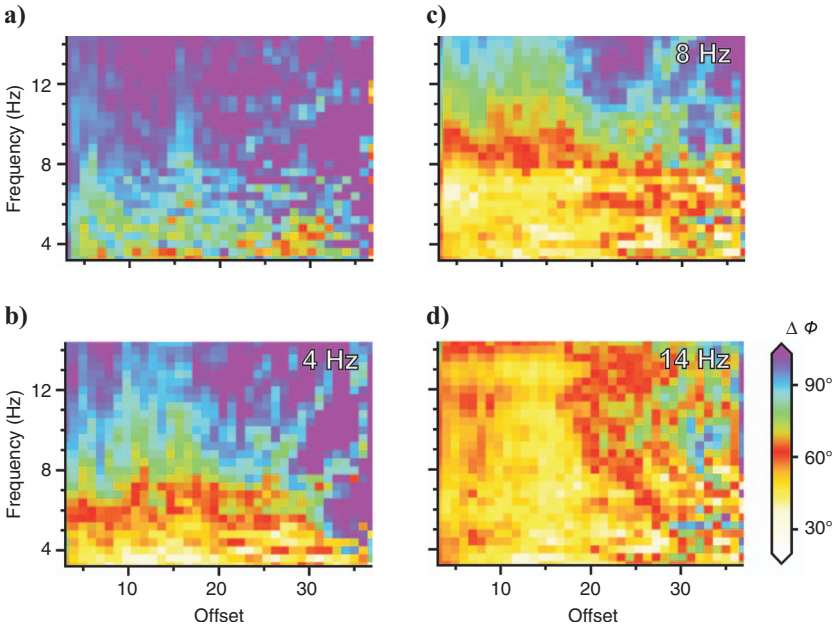

Figure 14. Root-mean-square-phase misfit as a function of offset and frequency for the inversion of the irregular-topography data with the implicit, weak surface boundary condition evaluated (a) for the starting model, (b) after inverting frequencies up to 4 Hz, (c) up to 8 Hz, and (d) for the final model of Figure 9d.

problems that we did not account for: our synthetics are noise-free, and they are in two dimensions. Investigating the influence of noise or 3D variations, however, is not the aim of this study. We took noise into account by not using frequencies below 3.2 Hz, the lowermost frequency used in the inversion of the real San Andreas fault data. The importance of 3D variations in this context is the potential impact of surface-scattered or converted waves. In our 2D model, we clearly ignore additional scattering and conversions from the sides. However, this is compensated by the different (linear versus cylindrical) spreading of surface waves in two dimensions. The main difference between our synthetics and 3D data is that energy converted and scattered at the surface is more coherent in two dimensions. However, if coherency of these phases has an impact on the results at all, it is rather to overestimate related artifacts.

CONCLUSIONS

The detrimental effects of ignoring the free surface in the inversion of P body waves are significant. This might be different if P-Rayleigh conversions and other surface-related phases could be removed from the data without damaging the wavelets, but that was not the purpose of this study. One surprising finding of our study is that these detrimental effects are largely independent of the topography. Strong topography produces additional scattering, and this scattering generally reduces the resolution if it is not accounted for. However, strong topography also destroys the coherency of multiples and mitigates reverberations, and the corresponding artifacts are reduced. This explains why in the layer-over-half-space part of the model, artifacts from ignoring the free surface are stronger for flat-surface data.

Our results also show that it is possible to mimic some effects of an irregular surface by a weak contrast along a staircase function, even if the wave propagator does not account for such heterogeneities. We obtained the best results using a 50% velocity reduction above the surface, but this value could depend on the method. The implicit boundary produces some amount of acoustic scattering and it mitigates wave propagation above ground, resulting in a significant increase of resolution. To also account for phase conversions at the free surface would require fully elastic inverse modeling, which is beyond the scope of this study. In general, our models show that acoustic full-waveform inversion is able to reconstruct much of the fine subsurface structure even in the presence of strong topography.

ACKNOWLEDGMENTS

The authors want to thank Gerhard Pratt and Johan Robertsson for making their codes available to us. We also thank Jean Virieux and two anonymous reviewers for helpful comments that improved this manuscript. Special thanks to Isabelle Lecomte for her very constructive editorial role. Shell International Exploration and Production B.V. provided support for this study.

REFERENCES

Barnes, C., and M. Charara, 2008, Full-waveform inversion results when using acoustic approximation instead of elastic medium: 70th Annual EAGE Conference and Exhibition, EAGE, Extended Abstracts, 27–35.

Bleibinhaus, F., J. A. Hole, T. Ryberg, and G. Fuis, 2007, Structure of the California coast ranges and San Andreas fault at SAFOD from seismic waveform inversion and reflection imaging: Journal of Geophysical Research, **112**, B06315, doi: 10.1029/2006JB004611.

Bleibinhaus, F., R. W. Lester, and J. A. Hole, 2009, Applying waveform inversion to wide-angle seismic surveys: Tectonophysics, **472**, 238–248.

Bohlen, T., and E. H. Saenger, 2006, Accuracy of heterogeneous staggered-grid finite-difference modeling of Rayleigh waves: Geophysics, **71**, no. 4, T109–T115.

Bunks, C., F. M. Saleck, S. Zaleski, and G. Chavent, 1995, Multiscale seismic waveform inversion: Geophysics, **60**, 1457–1473.

Choi, Y., D. J. Min, and C. Shin, 2008, Two-dimensional waveform inversion of multi-component data in acoustic-elastic coupled media: Geophysical Prospecting, **56**, 863–881.

Dougherty, M. E., and R. A. Stephen, 1988, Seismic energy partitioning and scattering in laterally heterogeneous ocean crust: Pure and Applied Geophysics, **128**, 195–229.

Gao, F., A. Levander, R. G. Pratt, C. A. Zelt, and G. L. Fradelizio, 2007, Waveform tomography at a groundwater contamination site: Surface reflection data: Geophysics, **72**, no. 5, G45–G55.

Gardner, G. H. F., L. W. Gardner, and A. R. Gregory, 1974, Formation velocity and density — Diagnostic basics for stratigraphic traps: Geophysics, **39**, 770–780.

Hicks, G. J., and R. G. Pratt, 2001, Reflection waveform inversion using local descent methods: Estimating attenuation and velocity over a gas-sand deposit: Geophysics, **66**, 598–612.

Hole, J. A., 1992, Nonlinear high-resolution three-dimensional seismic travel time tomography: Journal of Geophysical Research, **97**, 6553–6562.

Kamei, R., and R. G. Pratt, 2008, Waveform tomography strategies for imaging attenuation structure with cross-hole data: 70th Annual EAGE Conference and Exhibition, EAGE, Extended Abstracts, F019.

Levander, A. R., 1988, Fourth-order finite-difference *P-SV* seismograms: Geophysics, **53**, 1425–1436.

Malinowski, M., and S. Operto, 2008, Quantitative imaging of the Permo-Mesozoic complex and its basement by frequency domain waveform tomography of wide-aperture seismic data from the Polish Basin: Geophysical Prospecting, **56**, 805–825.

Nihei, K. T., and X. Y. Li, 2007, Frequency response modelling of seismic waves using finite difference time domain with phase sensitive detection (TD-PSD): Geophysical Journal International, **169**, 1069–1078.

Operto, S., C. Ravaut, L. Improta, J. Virieux, A. Herrero, and P. Dell'

Aversana, 2004, Quantitative imaging of complex structures from dense wide-aperture seismic data by multiscale traveltime and waveform inversions: A case study: Geophysical Prospecting, **52**, 625–651.
Operto, S., J. Virieux, J. X. Dessa, and G. Pascal, 2006, Crustal seismic imaging from multifold ocean bottom seismometer data by frequency domain full waveform tomography: Application to the eastern Nankai trough: Journal of Geophysical Research, **111**, B09306, doi: 10.1029/2005JB003835.
Pratt, R. G., 1999, Seismic waveform inversion in the frequency domain, Part 1: Theory and verification in a physical scale model: Geophysics, **64**, 888–901.
Pratt, R. G., C. Shin, and G. J. Hicks, 1998, Gauss-Newton and full Newton methods in frequency-space seismic waveform inversion: Geophysical Journal International, **133**, 341–362.
Pratt, R. G., Z. M. Song, P. Williamson, and M. Warner, 1996, Two-dimensional velocity models from wide-angle seismic data by wavefield inversion: Geophysical Journal International, **124**, 323–340.
Pratt, R. G., and M. H. Worthington, 1990, Inverse theory applied to multisource cross-hole tomography. Part 1: Acoustic wave-equation method: Geophysical Prospecting, **38**, 287–310.
Ravaut, C., S. Operto, L. Improta, J. Virieux, A. Herrero, and P. Dell' Aversana, 2004, Multiscale imaging of complex structures from multifold wide-aperture seismic data by frequency-domain full-waveform tomography: Application to a thrust belt: Geophysical Journal International, **159**, 1032–1056.
Robertsson, J. O. A., 1996, A numerical free-surface condition for elastic/viscoelastic finite-difference modeling in the presence of topography: Geophysics, **61**, 1921–1934.
Robertsson, J. O. A., J. O. Blanch, and W. W. Symes, 1994, Viscoelastic finite-difference modeling: Geophysics, **59**, 1444–1456.
Robertsson, J. O. A., and K. Holliger, 1997, Modeling of seismic wave propagation near the earth's surface: Physics of the Earth and Planetary Interiors, **104**, 193–211.
Sayles, R. S., and T. R. Thomas, 1978, Surface-topography as a nonstationary random process: Nature, **271**, 431–434.
Shin, C., and D. J. Min, 2006, Waveform inversion using a logarithmic wavefield: Geophysics, **71**, no. 3, R31–R42.
Virieux, J., S. Operto, H. Ben-Hadj-Ali, R. Brossier, V. Etienne, F. Sourbier, L. Giraud, and A. Haidar, 2009, Seismic wave modeling for seismic imaging: The Leading Edge, **28**, 538–544.